Title
Tunable C-Band Isolator Using Magnetized Gaseous Plasma

Journal
IEEE Transactions on Microwave Theory and Techniques, PP(99)

ISSN
0018-9480

Authors
Ewert, Armin
Sievenpiper, Daniel F

Publication Date
2026

DOI
10.1109/tmtt.2026.3689425

Tunable C-Band Isolator Using Magnetized Gaseous Plasma

Armin Ewert, *Graduate Student Member, IEEE*, and Daniel F. Sievenpiper, *Fellow, IEEE*

***Abstract*—This study presents a compact, tunable nonreciprocal microwave isolator based on a magnetized gaseous plasma column integrated into a rectangular waveguide. The device operates in the C-band and employs a partially metal-coated commercial low-pressure discharge lamp together with permanent magnets to provide axial magnetic bias. Nonreciprocal behavior arises from direction-dependent surface magnetoplasmons supported at the plasma-quartz interface. Experimental measurements demonstrate up to $10\ \mathrm{dB}$ isolation with approximately $2\ \mathrm{dB}$ insertion loss. The isolator exhibits tunability through plasma density, magnetic bias strength, and input microwave power, enabling dynamic control of the isolation band. A power-dependent increase in plasma density shifts the nonreciprocal band toward higher frequencies, providing an additional tuning mechanism under high-power operation. The proposed approach offers a passive, reconfigurable alternative to conventional ferrite and time-modulated isolators and is well suited for high-power C-band microwave systems.**

***Index Terms*—Microwave isolators, magnetized plasma, nonreciprocal**

I. Introduction

ISOLATORS are well-established microwave components. They enable electromagnetic energy to propagate in one direction while suppressing propagation in the opposite direction [1], [2], [3]. Isolators are widely used for transmitter protection, suppression of reflected power, and improvement of system stability in microwave systems.

Most practical isolators today rely on ferrites and are available as commercial off-the-shelf components. Simultaneously, there is a growing interest in chip-scale implementations that avoid magnetic materials. These approaches exploit non-magnetic nonreciprocity, for example, through spatio-temporal modulation [4]. Despite decades of development, nonreciprocal microwave devices remain an active research topic due to persistent trade-offs between isolation, insertion loss, bandwidth, power handling, tunability, and system complexity. Recent examples include circulators based on adiabatic flux modulation [5] and 3D-printed circulators [6]. Ferrite-based devices continue to demonstrate wideband and extreme isolation [7]. In the context of spatio-temporal modulation, research has focused on transmission lines [8] and bandpass filters [9].

Magnetized plasmas provide an alternative route to nonreciprocity. Early research concentrated on semiconductor plasmas for microwave isolators and circulators. These devices were experimentally demonstrated, but typically operated at higher frequencies and required cryogenic temperatures to reduce losses [10], [11], [12], [13], [14], [15].

Plasma can be realized not only in solid-state platforms but also in gaseous form, offering a flexible medium whose electromagnetic properties can be controlled through external parameters. When subjected to a static magnetic bias, gaseous plasma exhibits the same gyrotropic response and nonreciprocal behavior as solid-state plasmas. Based on this principle, circulators operating in the C-band using magnetized gaseous plasma have been experimentally demonstrated [16], [17]. In parallel, the scattering characteristics of magnetized plasma columns have been studied in detail, providing insight into the underlying wave–plasma interactions [18], [19]. More recently, nonreciprocal surface waves propagating along gaseous plasma columns have been reported [20]. Related plasma-based structures have also been shown to support nonreciprocal leaky-wave propagation under magnetic bias [21].

Compared to conventional solid-state and ferrite-based approaches, gaseous plasma offers unique advantages. These include self-healing behavior after high-power events, dynamic on/off operation through plasma generation and wide tunability of the plasma and electron cyclotron frequencies. These properties enable frequency agility, moderate-bandwidth operation, and high-power handling beyond what other approaches provide [22], [23].

No microwave isolator based on gaseous plasma has been reported to date. This work demonstrates a gaseous plasma microwave isolator operating in the C-band using commercial off-the-shelf equipment. Experimental measurements are presented and the performance is compared with ferrite-based, time-modulated, and spatio-temporally modulated isolators. Potential applications include high-power radar transmitters, communication systems, fusion plasma heating and industrial microwave processing.

II. Background

Applying a static magnetic field $\mathbf{B}_0$ along the y-axis transforms the plasma into a gyrotropic medium with an anisotropic permittivity tensor. The off-diagonal tensor elements break time-reversal symmetry and enable nonreciprocal wave propagation. For a cold, collisionless plasma, the relative permittivity tensor is given by [22], [23]

$$\underline{\boldsymbol{\varepsilon}}_{\boldsymbol{p}} = \begin{bmatrix} \varepsilon_t & 0 & -i\varepsilon_g \\ 0 & \varepsilon_a & 0 \\ i\varepsilon_g & 0 & \varepsilon_t \end{bmatrix} \tag{1}$$

where

$$\varepsilon_t = 1 - \frac{\omega_p^2}{\omega^2 - \omega_c^2}, \quad \varepsilon_a = 1 - \frac{\omega_p^2}{\omega^2}, \quad \varepsilon_g = \frac{\omega_c \omega_p^2}{\omega(\omega_c^2 - \omega^2)}$$

Manuscript received XX August 2026; revised XX September 20XX; accepted XX July 20XX. Date of publication XX August 20XX; date of current version 1 September 20XX. This research was supported by an Air Force Office of Scientific Research Multi-University Research Initiative (MURI) with Grant No. FA9550-21-1-0244.

Armin Ewert and Daniel F. Sievenpiper are with the Applied Electromagnetics Group at University of California San Diego: aewert@ucsd.edu, dsievenpiper@ucsd.edu

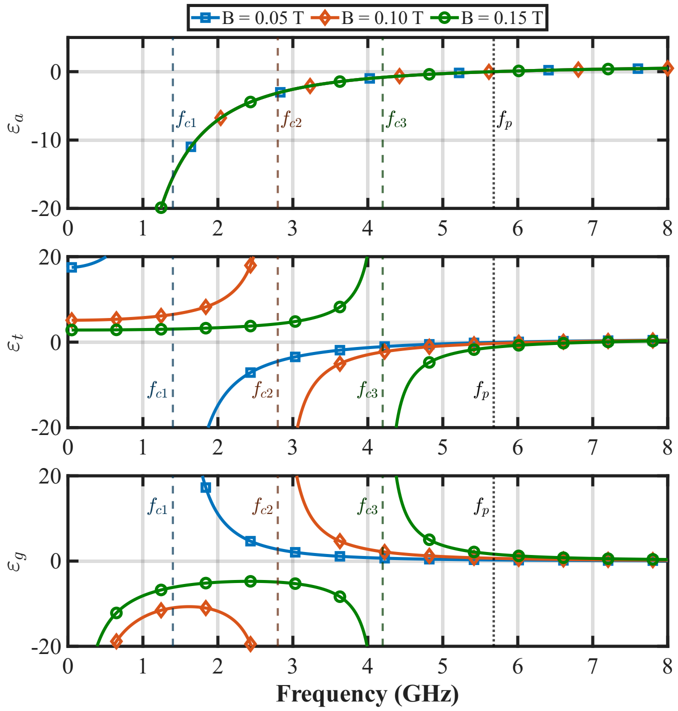

Fig. 1. Frequency dependence of the plasma permittivity tensor components ε_a, ε_t, and ε_g for different magnetic bias values ($B_0 = 0.05, 0.10$, and 0.15 T). The dashed lines indicate the corresponding cyclotron frequencies, while f_p denotes the plasma frequency. The magnetic bias shifts the resonance behavior of ε_t and ε_g, thereby defining the operating regime for nonreciprocal surface wave propagation.

Here, $\omega_p = \sqrt{n_e e^2/(m_e \varepsilon_0)}$ is the electron plasma frequency and $\omega_c = eB_0/m_e$ is the electron cyclotron frequency. The axial component ε_a follows a Drude-type response and is independent of the magnetic bias, whereas the transverse component ε_t exhibits a resonance near the cyclotron frequency due to magnetization [23], [24]. The off-diagonal component ε_g introduces gyrotropy and breaks time-reversal symmetry, leading to directional resonances. In the Voigt configuration, this results in nonreciprocal surface wave propagation and the formation of a frequency bandgap that scales with the cyclotron frequency ω_c. Within this bandgap, waves propagate in one direction while being strongly suppressed in the opposite direction [3], [25].

The frequency dependence of the permittivity tensor components is shown in Fig. 1 for different magnetic bias values. The cyclotron frequency shifts with B_0, which in turn modifies the resonance of ε_t and the magnitude of ε_g. As a result, both the location and width of the nonreciprocal bandgap can be tuned through the applied magnetic bias.

These features define the operating regime of the device. In particular, the resonance and sign change of ε_t, together with the strength of ε_g, determine the frequency range in which nonreciprocal surface waves can exist. The relative position of the cyclotron and plasma frequencies therefore directly controls the location and width of the nonreciprocal bandgap observed in the dispersion relation.

The dispersion relation of these nonreciprocal surface waves can be expressed using the Voigt permittivity $\varepsilon_V = (\varepsilon_t^2 - \varepsilon_g^2)/\varepsilon_t$ [26], [27] as

$$\sqrt{k_z^2 - \frac{\omega^2}{c^2}} + \frac{\sqrt{k_z^2 - \frac{\omega^2}{c^2}\varepsilon_V}}{\varepsilon_V} = \frac{\varepsilon_g k_z}{\varepsilon_t \varepsilon_V} \tag{2}$$

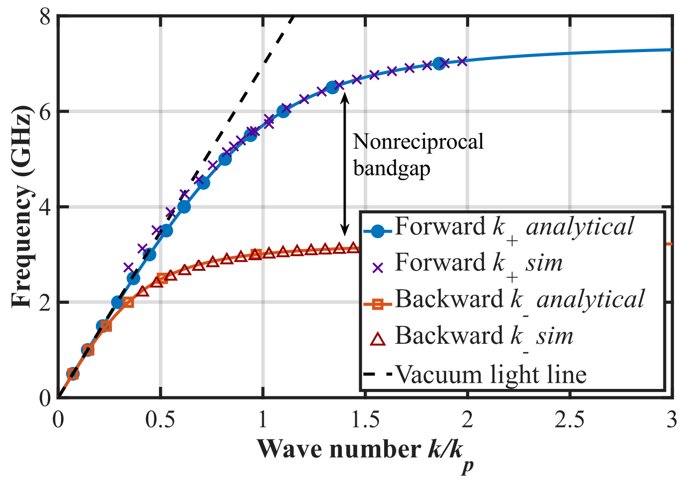

Fig. 2. Analytical dispersion relation from (2) compared with eigenmode simulations performed in COMSOL Multiphysics.

Figure 2 shows the dispersion relation of surface magnetoplasmons (SMPs). The forward and backward branches are asymmetric. A nonreciprocal bandgap between 3.5 and 7 GHz is observed. In this range, slow-wave surface modes exist only for one propagation direction. In addition to the analytical model, the eigenmodes were obtained from full-wave simulations in COMSOL Multiphysics, showing good agreement with the theoretical dispersion. The SMP resonance frequencies are given by [25]

$$\omega_{\pm} = \frac{1}{2}\left(\pm\omega_c + \sqrt{2\omega_p^2 + \omega_c^2}\right). \tag{3}$$

These direction-dependent surface modes couple to the electromagnetic fields of the waveguide. They are responsible for the observed nonreciprocal scattering from a magnetized plasma column [18]. This scattering mechanism forms the physical basis of the proposed isolator.

A magnetized plasma column placed symmetrically in a waveguide typically does not yield net nonreciprocity. The supported surface wave circulates clockwise for one bias direction and counterclockwise for the opposite. The overall response remains reciprocal.

Partial metallization of the plasma column, as illustrated in Fig. 3, fundamentally alters this behavior. Surface waves can no longer propagate around the conducting side. Propagation is restricted to the exposed plasma surface. When surface waves are supported in only one direction, the propagation becomes unidirectional. This breaks reciprocity and enables isolation.

III. Model

The device geometry is shown in Fig. 3. It is implemented in a standard WR-187 rectangular waveguide with inner dimensions of 47.55 mm $\times$ 22.15 mm. The dominant TE_{10} mode

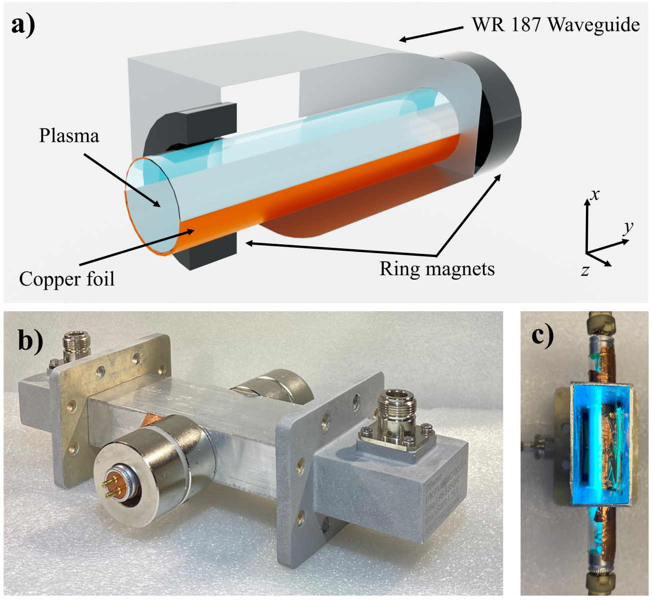

Fig. 3. Model of the isolator: (a) schematic view, (b) isometric photograph, and (c) photograph in the $xy-$plane with plasma turned on

has a cutoff frequency of 3.153 GHz. The waveguide operates from 3.95 to 5.85 GHz.

Figure 3(a) shows a schematic of the waveguide section. A plasma column is placed perpendicular to the propagation direction and to the electric field of the TE_{10} mode. The column is vertically offset and touches the bottom wall of the waveguide. Its lower half is covered with a conducting layer made of copper foil. The conducting coating suppresses surface-wave propagation along the covered side of the plasma column.

The plasma is generated inside a commercial Ushio G4T5 germicidal lamp. The quartz envelope has a relative permittivity of $\varepsilon_r = 3.8$, an outer diameter of 16 mm, and a wall thickness of 0.5 mm. The tube length is 130 mm. The lamp is filled with argon and doped with mercury droplets. Tungsten filaments at both ends are heated using a 2 V DC supply to assist ignition. A 37 kHz electronic ballast delivers 4 W of AC power to sustain a stable discharge. The gas pressure inside the discharge lamp is approximately 250 Pa, consistent with values reported for similar low-pressure plasma discharges in [28], and is an important parameter governing the electron-neutral collision frequency and associated losses. The plasma density is estimated as approximately $n_e = 4 \times 10^{17}\ \mathrm{m}^{-3}$ based on previously reported measurements for similar low-pressure gaseous plasma elements operated under comparable conditions [28], [29]. Among these, [29] is particularly relevant because it reports a detailed mapping between ballast bias voltage and plasma density, which is in good agreement with the density value adopted in this work.

The chosen plasma density corresponds to a plasma frequency close to the upper edge of the operating band. This is intentional, as strong interaction between the electromagnetic wave and the plasma occurs when the operating frequency approaches the plasma frequency. However, in practice the plasma is not homogeneous and exhibits a radial density gradient, with the maximum density occurring near the center of the discharge and lower density toward the quartz boundary. As a result, the effective plasma frequency experienced by the guided wave is lower than the peak value estimated from the central density.

The plasma density chosen is the lowest achievable value for the given discharge, as it is set by the minimum stable bias voltage of the ballast in constant-voltage (CV) operation. Lower densities could not be reliably sustained under these conditions, which imposes a practical constraint on the device design.

The position of the plasma frequency relative to the operating band has a direct impact on device performance. For $\omega_p \ll \omega$, the plasma response is weak, resulting in reduced nonreciprocal interaction and low isolation. For $\omega_p \gg \omega$, the plasma behaves increasingly like a lossy conductor, leading to higher insertion loss. An optimal regime is therefore obtained when the plasma frequency is close to, but slightly above, the operating frequency range, where strong nonreciprocal effects can be achieved while maintaining moderate loss. This trade-off determines the achievable isolation and insertion loss and provides a guideline for selecting plasma parameters in practical implementations.

An axial magnetic bias field B_0 is applied using four N42 neodymium ring magnets. The magnets have an outer diameter of 38 mm, an inner diameter of 19 mm, and a thickness of 19 mm. They are placed outside the waveguide and surround the plasma tube. Hall probe measurements and electromagnetic simulations confirm an effective magnetic field of approximately 100 mT across the center of the plasma volume. The simulated field distribution is shown in Appendix A.

The experimental realization is shown in Fig. 3(b) and (c). The waveguide is machined from aluminum and conforms to WR-187 dimensions. SMA-to-waveguide adapters connect the device to a vector network analyzer for low-power S-parameter measurements at -10 dBm. For high-power characterization, external power amplifiers and power meters are used.

Full-wave simulations are performed using the modal solver in Ansys HFSS. The plasma is modeled as a homogeneous, dispersive medium described by the gyrotropic permittivity tensor given in (1).

IV. Results

A. S-Parameters

Figure 4 shows the simulated and measured S-parameters in the C-band. The forward transmission S_{21} and reverse transmission S_{12} differ, confirming nonreciprocal behavior. At 4.2 GHz, the isolator achieves approximately 10 dB isolation with an insertion loss of about 2 dB.

The measured S_{12} shows slightly stronger isolation than predicted by simulation over part of the band. This discrepancy is mainly attributed to the simplified plasma model used in the full-wave analysis. In HFSS, the plasma is represents a fundamental trade-off between strong nonreciprocal interaction and dissipative loss. In practice, the plasma exhibits

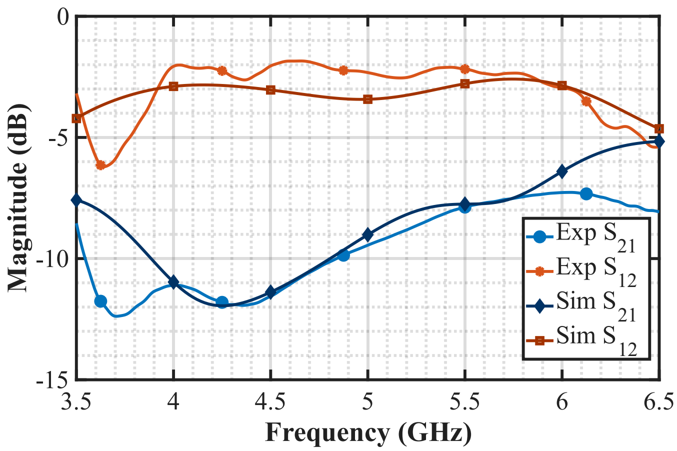

Fig. 4. Measured and simulated S-parameters with a magnetic bias of 100 mT at the center of the plasma column.

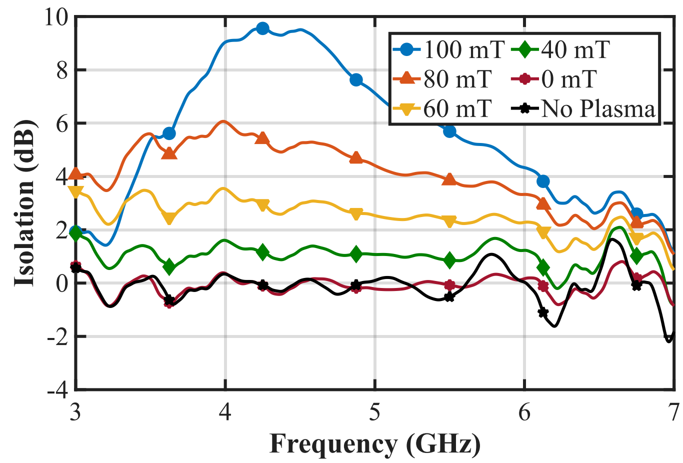

Fig. 5. Measured isolation as a function of magnetic field strength at the center of the plasma column.

radial and axial density gradients, with the highest density near the center of the discharge and reduced density toward the quartz wall. In addition, the magnetic field generated by the permanent magnets is not perfectly uniform over the full plasma volume. These nonuniformities modify the local gyrotropic response and can enhance the effective nonreciprocal interaction compared to the idealized homogeneous model. As a result, the experiment can exhibit slightly stronger reverse-wave suppression than predicted by simulation. Despite these effects, the simulated and measured responses show the same overall trend and agree well in terms of the operating band and level of nonreciprocity.

To quantify the operating bandwidth, we define it as the frequency range over which the isolation exceeds 6 dB while maintaining an insertion loss below 3 dB. From the experimental results in Fig. 4, this condition is satisfied approximately between 3.9 GHz and 5.5 GHz, corresponding to an absolute bandwidth of 1.6 GHz. This yields a fractional bandwidth of approximately 34% with respect to the center frequency of 4.7 GHz.

The effect of magnetic bias on isolation is shown in Fig. 5. Isolation increases monotonically with the applied magnetic field. This trend confirms that stronger magnetic bias enhances the nonreciprocal response.

To further clarify the role of plasma losses, a parametric study of the collision frequency ν_c was performed, as shown in Fig. 6 and Fig. 7. The collision frequency is directly related to the gas pressure and represents the dominant dissipative mechanism in the plasma. A strictly lossless case with $\nu_c = 0$ was not included, because it led to nonphysical numerical behavior and poor convergence in the HFSS simulations.

As ν_c increases, the plasma becomes more lossy, which reduces the achievable isolation and modifies the insertion loss. For low collision frequencies ($\nu_c = 0.2$–1 GHz), strong and narrow isolation peaks are obtained. At higher collision frequencies ($\nu_c = 4$–10 GHz), the isolation level decreases and the response becomes smoother and broader. This behavior is consistent with increased damping of the magnetoplasmon resonance: higher collision frequency lowers the effective quality factor of the resonance, which reduces the peak isolation but

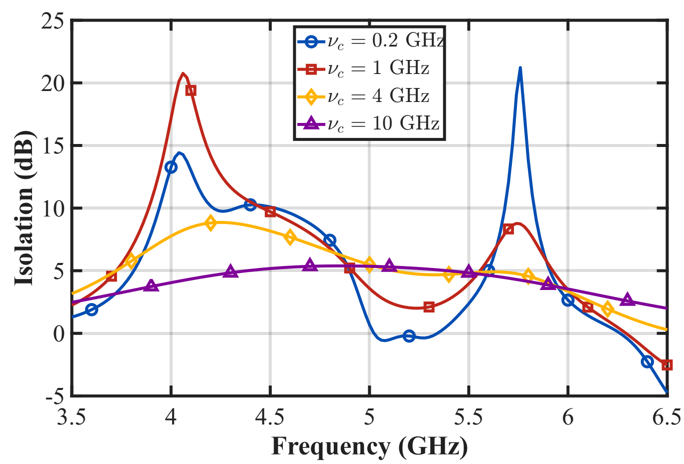

Fig. 6. Simulated isolation versus frequency for different plasma collision frequencies.

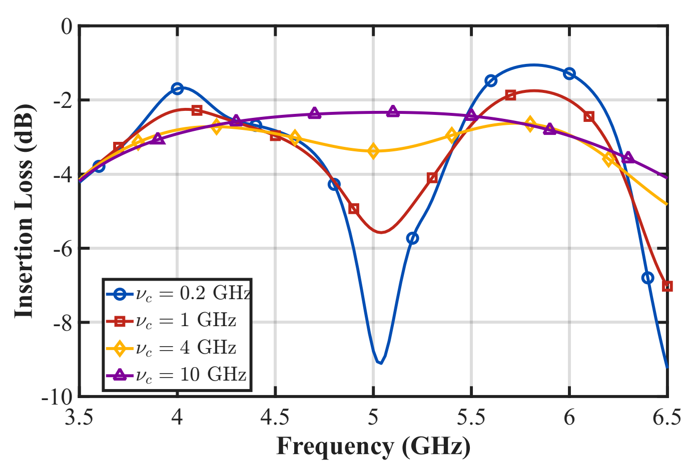

Fig. 7. Simulated insertion loss versus frequency for different plasma collision frequencies.

increases the bandwidth. This reduction in quality factor leads to broader but weaker resonances.

By comparison with the measured response in Fig. 4, the experimental plasma is consistent with an effective collision

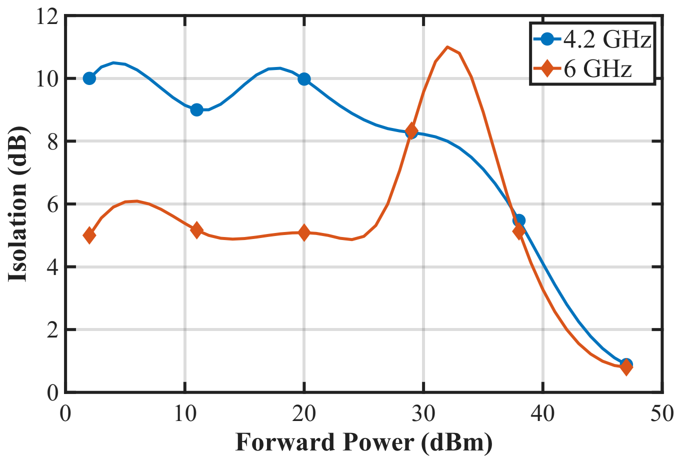

Fig. 8. Measured isolation versus input power at 4.2 and 6 GHz.

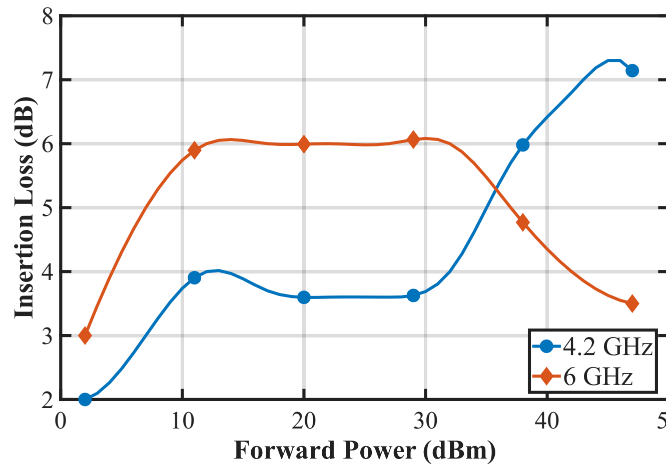

Fig. 9. Measured insertion loss versus input power at 4.2 and 6 GHz.

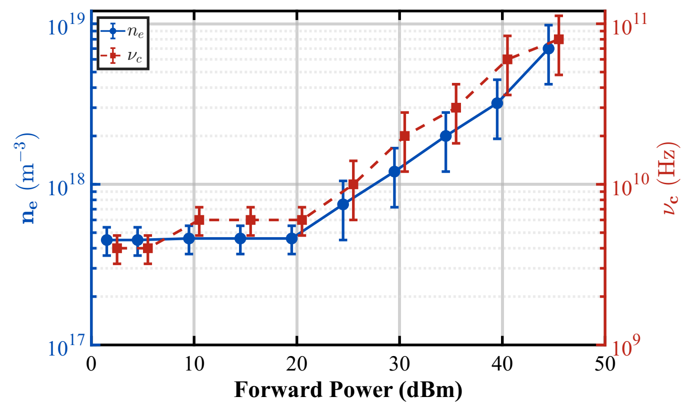

Fig. 10. Derived plasma density and collision frequency as a function of input microwave power, obtained by matching measured isolation and insertion loss to HFSS simulations.

frequency on the order of 4 GHz. Overall, these results show that the operating point represents a trade-off between strong nonreciprocal interaction and dissipative loss, and they highlight the importance of gas pressure and discharge conditions in optimizing device performance.

B. Power measurement

Figure 8 shows the measured isolation as a function of input power at 4.2 and 6 GHz. The magnetic bias is fixed at 100 mT. At 4.2 GHz, isolation decreases with increasing input power. At 6 GHz, isolation increases and reaches a maximum at higher power levels.

This behavior is attributed to a power-dependent increase in plasma density. Higher microwave power modifies the plasma discharge and leads to an increase in the effective electron density. As a result, the nonreciprocal band shifts toward higher frequencies. By selecting an initial plasma density below the optimum value, the density increase with power aligns the nonreciprocal band with the operating frequency.

The measured insertion loss versus input power is presented in Fig. 9. At 4.2 GHz, the insertion loss increases with power. The rising plasma density drives the effective permittivity further negative. The plasma therefore behaves more like a lossy conductor, increasing attenuation. At 6 GHz, the behavior differs. The insertion loss initially increases and then saturates. Above 30 dBm, it decreases with further power increase. These trends are consistent with the isolation behavior shown in Fig. 8.

The plasma density and collision frequency shown in Fig. 10 are extracted by mapping the measured isolation and insertion loss in Figs. 8 and 9 to HFSS simulations. Specifically, for each input power level, the plasma parameters are identified that reproduce the measured device response.

At low input powers below 25 dBm, both the plasma density and collision frequency remain approximately constant, indicating that the plasma is primarily sustained by the discharge power. Once the input microwave power becomes comparable to the discharge power ($\sim$ 4 W), a pronounced increase in both parameters is observed. At 1 W input power, the plasma density increases by approximately a factor of two. This increase is consistent with the observed shift of the nonreciprocal band toward higher frequencies in Fig. 8, and agrees with reported power-dependent plasma behavior in [30].

The extracted collision frequencies are also in good agreement with values reported in [31]. The error bars reflect the range of plasma parameters that yield similar isolation and insertion loss, highlighting the inherent trade-off between plasma density and collision frequency in determining device performance.

A full multiphysics model of the plasma is not included, as the discharge behavior depends on several coupled factors, including gas pressure, excitation conditions, and microwave power.

The reduced isolation observed at high input powers (e.g., 40 dBm) can be attributed to the combined effect of increased plasma density and enhanced collisional losses. As shown in Fig. 10, the plasma density rises significantly with input power, shifting the nonreciprocal band toward higher frequencies. At sufficiently high power levels, the isolation band shifts toward the upper limit of the single-mode TE_{10} regime and beyond the optimal operating range. Consequently, strong isolation is no longer observed within the measured frequency range.

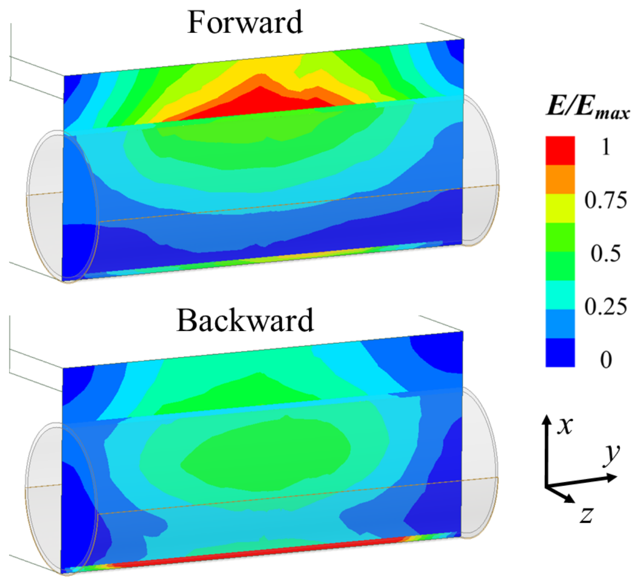

Fig. 11. Normalized complex electric field magnitude in the $E-$plane at 4.2 GHz for forward and backward excited waves.

At the same time, the extracted collision frequency increases with input power, leading to stronger damping of the magnetoplasmon resonance. This increased dissipation reduces the achievable isolation and increases the insertion loss, resulting in an overall degradation of device performance.

In addition, at higher frequencies and elevated plasma densities, weak contributions from higher-order mode excitation or mode conversion may occur, which may further reduce the measured isolation. Overall, the observed behavior reflects a transition from a strongly nonreciprocal regime to a loss-dominated regime at high input power. This indicates that the performance limitation at high power is not due to device breakdown, but rather due to a shift of the operating point outside the designed frequency range combined with increased dissipative loss.

C. Fields

The normalized complex electric field magnitude in the E-plane at 4.2 GHz is shown in Fig. 11. Results are shown for forward $(+k_z)$ and backward $(-k_z)$ excitation. In the forward direction, transmission occurs. The field follows the exposed plasma surface along the upper side of the column. In the backward direction, transmission is strongly suppressed. The field attempts to propagate below the column, where the conducting coating blocks the path and causes strong attenuation.

The nonreciprocal surface waves supported by the magnetized plasma prevent backward propagation along the exposed interface. The fundamental TE_{10} mode is significantly perturbed in both directions. Strong field concentration appears at the quartz-conductor interface. This effect is more pronounced for backward excitation.

V. Discussion and Conclusion

This work demonstrates a compact and tunable nonreciprocal microwave isolator in the C-band based on a magnetized plasma column integrated into a rectangular waveguide. It combines a partially metal-coated commercial low-pressure discharge lamp with permanent magnets to provide axial magnetic bias.

Nonreciprocal operation arises from direction-dependent surface magnetoplasmons supported at the plasma-quartz interface. The conducting coating applied to half of the plasma column suppresses surface-wave propagation along the covered side. As a result, waves are forced to propagate only along the exposed plasma surface. Under axial magnetic bias, these surface modes are inherently nonreciprocal. Transmission is therefore allowed in one direction and strongly suppressed in the opposite direction.

Experimental measurements show up to 10 dB isolation with approximately 2 dB insertion loss. The proposed gaseous plasma-based isolator offers several distinct advantages for practical systems.

First, it provides continuous tunability through plasma density, magnetic bias, and input power, enabling dynamic control of the isolation band without structural modification. Second, gaseous plasma supports high-power operation and exhibits self-healing behavior after high-power events. Third, the implementation is simple and passive, requiring no time modulation or active circuitry. In addition, the plasma can be switched off, restoring near-transparent waveguide operation and enabling reconfigurable functionality. Finally, the approach avoids magnetic materials, reducing weight and integration constraints, and is not inherently limited to a specific frequency range.

These features highlight that the proposed device targets a different operating space compared to ferrite-based isolators, where tunability, reconfigurability, and high-power robustness are prioritized over maximum isolation and minimum insertion loss.

Numerical simulations are in good agreement with the measurements. Isolation increases with magnetic bias strength. Field distributions confirm that energy follows the exposed plasma surface in the forward direction and is strongly attenuated in the backward direction.

An additional tuning mechanism arises from the power-dependent plasma density. Increasing input power raises the electron density and shifts the nonreciprocal band toward higher frequencies. This effect enables performance optimization at the desired operating frequency under high-power conditions and provides adaptive control of the isolation band without modifying the device geometry.

The high-power capability of the device was experimentally verified up to an input power of 47 dBm without any observable damage or performance degradation of the plasma element. At this power level, a shift of the isolation band toward higher frequencies is observed, which is attributed to the increase in plasma density with input power. As a result, the isolation at the fixed operating frequencies decreases at higher power levels, as discussed in Section IV. For this reason,

TABLE I
COMPARISON

Method	Integration type	Tunability	Power handling	Isolation	Insertion loss	Frequency	Reference
Magn. gaseous plasma	Isolator, WR187	$n_e,\ B_0$	High, tunable	10 dB	2 dB	4-6 GHz	This work
Magn. gaseous plasma	Circulator, WR187	$n_e,\ B_0$	High, tunable	20 dB	5 dB	4-6 GHz	[17]
Magn. gaseous plasma	Circulator, WR229	$n_e,\ B_0$	High, tunable	15 dB	5 dB	3-5 GHz	[16]
Magn. semiconductor (300 K)	Isolator, WR42	B_0	Medium	15 dB	3 dB	18-26 GHz	[11]
Magn. semiconductor (77 K)	Circulator, WR15	B_0	Medium	10 dB	10 dB	50-75 GHz	[15]
Ferrite	Isolator, WR187	B_0	High	21 dB	0.1 dB	4.2-5 GHz	[32]
Ferrite SMP	Isolator, SMA	B_0	Medium	80 dB	4 dB	2.4-3 GHz	[7]
Time-modulation	Circulator, SMA	V_{DC}	Low	55 dB	3.3 dB	0.95-1.05 GHz	[9]
Time-modulation	Isolator, SMA	f_m	Low	20 dB	3 dB	22-28 GHz	[8]

higher input power levels were not further pursued, as the device operation moves outside the designed frequency range rather than being limited by material breakdown.

The maximum applied power in this study was also limited by the available measurement setup. However, from a physical standpoint, gaseous plasma does not suffer from irreversible breakdown in the same way as solid-state or ferrite-based devices. Instead, it exhibits a self-healing behavior, where the plasma recombines and re-forms after high-power excitation. The primary limitation is therefore expected to arise from thermal effects in the surrounding materials (e.g., quartz envelope and waveguide walls) and from discharge stability, rather than from intrinsic damage to the plasma itself.

These observations indicate that the proposed device is well suited for high-power operation, with the practical limit determined by system-level constraints rather than by the plasma medium.

Compared to other nonreciprocal approaches, the proposed gaseous plasma isolator occupies a complementary operating regime. Ferrite-based devices provide higher isolation and lower insertion loss but lack tunability and often require bulky magnetic structures. Semiconductor plasma devices typically operate at higher frequencies and may require cryogenic conditions. Time-modulated approaches rely on active circuitry and increased system complexity. In contrast, gaseous plasma offers a lightweight, passive, and reconfigurable platform with high power robustness and inherent self-healing capability.

The device features three independent tuning parameters: plasma density (controlled by discharge conditions), magnetic bias strength, and input microwave power. The power-dependent density shift enables dynamic adjustment of the isolation band. While this study focuses on the microwave regime, the underlying physical mechanisms are not frequency-specific, and the same principles are expected to extend to other frequency regimes.

In summary, this work presents a simple and low-cost gaseous plasma-based microwave isolator that combines moderate isolation, moderate bandwidth, high power handling, and multiple tuning mechanisms. It is particularly well suited for applications requiring robust and adjustable nonreciprocal protection, such as high-power radar transmitters, communication systems, fusion plasma heating, and industrial microwave processing.

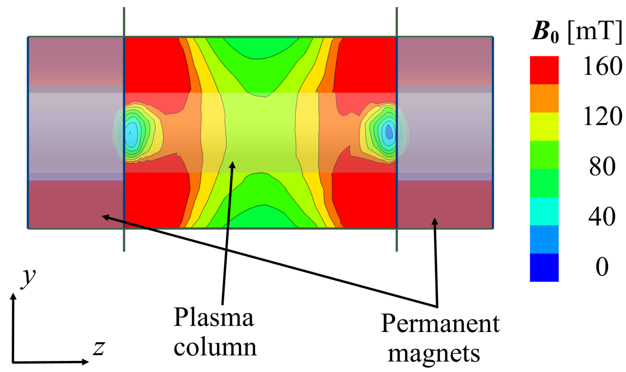

Fig. 12. Magnetic field magnitude along the y-axis produced by the ring magnet assembly.

APPENDIX A
MAGNETIC BIAS

Figure 12 shows the simulated magnetic field magnitude in the yz-plane generated by the ring magnet assembly. Hall probe measurements confirm the simulated field distribution. The results are consistent with magnetic field profiles reported for a similar magnet configuration in [17].

In the central region of the waveguide, where the TE_{10} mode field is strongest, the magnetic field magnitude is approximately $100\ \mathrm{mT}$. Closer to the waveguide walls, the field increases to about $150\ \mathrm{mT}$. As a result, the effective magnetic bias experienced by most of the guided power is close to $100\ \mathrm{mT}$.

REFERENCES

[1] D. M. Pozar, *Microwave engineering*. Hoboken, NJ: Wiley, fourth edition. ed., 2012.
[2] A. Kord, D. L. Sounas, and A. Alu, "Microwave nonreciprocity," *Proceedings of the IEEE*, vol. 108, p. 1728–1758, Oct. 2020.
[3] V. S. Asadchy, M. S. Mirmoosa, A. Díaz-Rubio, S. Fan, and S. A. Tretyakov, "Tutorial on electromagnetic nonreciprocity and its origins," *Proceedings of the IEEE*, vol. 108, no. 10, pp. 1684–1727, 2020.
[4] A. Nagulu and H. Krishnaswamy, "Non-magnetic non-reciprocal microwave components — state of the art and future directions," *IEEE Journal of Microwaves*, vol. 1, p. 447–456, jan 2021.
[5] M. Demarets, A. M. Vadiraj, C. Caloz, and K. D. Greve, "Broadband magnetless isolator using adiabatic flux modulation," *arXiv preprint arXiv:2509.24551*, sep 2025.
[6] V. Laur, J. P. Gouavogui, and B. Balde, "C-band hybrid 3-d-printed microwave isolator," *IEEE Transactions on Microwave Theory and Techniques*, vol. 69, p. 1579–1585, mar 2021.

[7] T. Jiang, D. Liang, H. Liang, L. Zou, T. Zhou, S. Li, and L. Shen, "Wideband isolator based on one-way surface magnetoplasmons with ultra-high isolation," *Scientific Reports*, vol. 14, p. 17474, july 2024.

[8] A. Nagulu, T. Dinc, Z. Xiao, M. Tymchenko, D. L. Sounas, A. Alù, and H. Krishnaswamy, "Nonreciprocal components based on switched transmission lines," *IEEE Transactions on Microwave Theory and Techniques*, vol. 66, p. 4706–4725, nov 2018.

[9] A. Kord, D. L. Sounas, and A. Alù, "Magnet-less circulators based on spatiotemporal modulation of bandstop filters in a delta topology," *IEEE Transactions on Microwave Theory and Techniques*, vol. 66, p. 911–926, feb 2018.

[10] R. Dinger and D. White, "The use of a thin vacuum-deposited insb film as a k-band field displacement isolator," *Proceedings of the IEEE*, vol. 60, p. 646–647, may 1972.

[11] K. Suzuki, "Room temperature solid-state plasma nonreciprocal microwave devices," *IEEE Transactions on Electron Devices*, vol. 16, p. 1018–1021, dec 1969.

[12] K. Suzuki and R. Hirota, "Nonreciprocal millimeter-wave devices using a solid-state plasma at room temperature," *IEEE Transactions on Electron Devices*, vol. 18, p. 408–411, july 1971.

[13] C. Yong, R. Sloan, and L. Davis, "A ka-band indium-antimonide junction circulator," *IEEE Transactions on Microwave Theory and Techniques*, vol. 49, p. 1101–1106, june 2001.

[14] S. S. Alshannaq and R. G. Rojas, "Millimeter wave isolator based on thin film magnetized semiconductors in fully-planar waveguide," in *Proceedings of the Fourth European Conference on Antennas and Propagation*, p. 1–3, apr 2010.

[15] Z. Ng, L. Davis, and R. Sloan, "Measurements of v-band n-type insb junction circulators," *IEEE Transactions on Microwave Theory and Techniques*, vol. 52, p. 482–488, feb 2004.

[16] H. Mehrpour Bernety, L. S. Houriez, J. A. Rodríguez, B. Wang, and M. A. Cappelli, "A tunable microwave circulator based on a magnetized plasma as an active gyrotropic element," *Physics of Plasmas*, vol. 29, p. 112114, nov 2022.

[17] F. Li, R. J. Davis, S. M. Kandil, and D. F. Sievenpiper, "Electromagnetic nonreciprocity in a magnetized plasma circulator," *Physical Review Applied*, vol. 18, p. 064066, Dec. 2022.

[18] L. S. Houriez, H. Mehrpour Bernety, J. A. Rodríguez, B. Wang, and M. A. Cappelli, "Experimental study of electromagnetic wave scattering from a gyrotropic gaseous plasma column," *Applied Physics Letters*, vol. 120, p. 223101, 06 2022.

[19] H. Mehrpour Bernety and M. A. Cappelli, "An electromagnetic scattering approach to identifying topological and non-topological unidirectional edge states at gyrotropic plasma interfaces," *Journal of Applied Physics*, vol. 133, p. 104902, 03 2023.

[20] H. Mehrpour Bernety, D. Murphy Zink, D. Piriaei, and M. A. Cappelli, "Experimental detection of topological surface waves at a magnetized plasma interface in the voigt configuration," *Applied Physics Letters*, vol. 124, p. 043102, Jan. 2024.

[21] A. Ewert and D. F. Sievenpiper, "Nonreciprocal time-invariant leaky waves enabled by magnetized plasma," *Authorea Preprints*, 2025.

[22] Y. Raizer, J. Allen, and V. Kisin, *Gas Discharge Physics*. Springer Berlin Heidelberg, 2011.

[23] J. A. Bittencourt, *Fundamentals of Plasma Physics*. Fundamentals of Plasma Physics, Third Edition by J.A. Bittencourt. Published by Springer-Verlag, New York, Inc.; 2004. ISBN 0-387-20975-1., third ed., 2004.

[24] K. Shastri, M. I. Abdelrahman, and F. Monticone, "Nonreciprocal and topological plasmonics," *Photonics*, vol. 8, p. 133, Apr. 2021.

[25] A. D. Boardman, *Electromagnetic surface modes*. Chichester: Wiley, 1982.

[26] A. R. Davoyan and N. Engheta, "Theory of wave propagation in magnetized near-zero-epsilon metamaterials: Evidence for one-way photonic states and magnetically switched transparency and opacity," *Physical Review Letters*, vol. 111, p. 257401, Dec. 2013.

[27] J. J. Brion, R. F. Wallis, A. Hartstein, and E. Burstein, "Theory of surface magnetoplasmons in semiconductors," *Physical Review Letters*, vol. 28, p. 1455–1458, May 1972.

[28] R. Lee, B. Wang, and M. A. Cappelli, "Plasma modification of spoof plasmon propagation along metamaterial-air interfaces," *Applied Physics Letters*, vol. 111, p. 261105, dec 2017.

[29] J. A. Rodríguez and M. A. Cappelli, "Inverse design and experimental realization of plasma metamaterials," *Physical Review Applied*, vol. 20, p. 044017, oct 2023.

[30] R. Liu, J. Peng, L. Lin, D. Qiu, Z. Liu, and Q. Lin, "Factors influencing the electromagnetic transmission of mercury vapor discharge plasma tube arrays," *Physica Scripta*, vol. 98, p. 055611, apr 2023.

[31] Y. Liu and Z. Hou, "Diagnostics of plasma electron density and collision frequency of fluorescent lamp using microwave transmission diagnostics," *Journal of Physics: Conference Series*, vol. 1324, p. 012073, oct 2019.

[32] Exceed Microwave, *ISO-W-4600-800-187 WR187 Waveguide Isolator Datasheet*, jun 2019. Datasheet [Online].

Armin Ewert earned his B.S. in mathematical engineering and his M.S. in electrical engineering from Bundeswehr University Munich in 2018 and 2019 respectively. He has served in the German Air Force as an engineer where he developed and optimized combat aircraft communication modules. In 2023 he joined the Applied Electromagnetics Group at UC San Diego in La Jolla, CA where he is currently pursuing his Ph.D. His research interests include the electromagnetic topology in magnetized plasma with a focus on electromagnetic nonreciprocity.

Daniel F. Sievenpiper (M'94–SM'04–F'09) received his B.S. and Ph.D. in electrical engineering from the University of California, Los Angeles, USA, in 1994 and 1999, respectively. Dan joined HRL Laboratories in Malibu, CA in 1999. During the following 11 years, he and his team developed new electromagnetic structures with an emphasis on small, conformal, tunable, and steerable antennas. Dan held a variety of technical and management positions at HRL including Director of the Applied Electromagnetics Laboratory. In 2010 he joined UC San Diego as a professor in the Electrical and Computer Engineering Department, where his research is focused on artificial media, and the integration of active electronics with electromagnetic structures and antennas to enable new capabilities and applications. His recent work involves anisotropic and active metasurfaces, photonic and phononic topological insulators, small and wearable antennas, and biological applications of electromagnetics. In 2008, Dan received the URSI Issac Koga Gold Medal, and also the IEEE Antennas and Propagation Society Piergiorgio Uslenghi Letters Prize Paper Award. In 2009, he was named as a Fellow of the IEEE, and in 2019, he was awarded the John D. Kraus Antenna Award. During 2010-2017, Dan served as an associate editor of IEEE Antennas and Wireless Propagation Letters. He also served as the chair of the IEEE Antennas and Propagation Society Administrative Committee on New Technology Directions from 2013-2014, and as the general chair of the IEEE Antennas and Propagation Symposium and URSI Radio Science Meeting which was held in San Diego in 2017. He served as the vice chair of the UCSD Electrical and Computer Engineering Department from 2019-2024, and on the UCSD Admissions Committee from 2024-present. Dan currently has more than 80 issued patents and more than 200 publications.